ORIGINAL RESEARCH ARTICLE

Open Access

Application-based design of the Fresnel lens solar concentrator

Hassan Qandil[1], Shuping Wang[2] and Weihuan Zhao[1*]

Abstract

A novel genetically themed hierarchical algorithm (GTHA) has been investigated to design Fresnel lens solar concentrators that match with the distinct energy input and spatial geometry of various thermal applications. Basic heat transfer analysis of each application decides its solar energy requirement. The GTHA incorporated in MATLAB® optimizes the concentrator characteristics to secure this energy demand, balancing a minimized geometry and a maximized efficiency. The optimum concentrator is then simulated to ensure the algorithm validity. To verify the algorithmic-optimization and simulation-validation processes, two experimental applications were selected from the literature, a solar welding system for H13 steel plates and a solar Stirling engine with an aluminum-cavity receiver attached to the heater section. In each case, a flat Fresnel lens with a spot focus was algorithmically designed to supply the desired solar heat, and then a computer simulation of the optimized lens was conducted showing great comparability to the original experimental results.

Keywords: Fresnel lens, Concentrated solar energy, Solar welding, Stirling engine, Algorithmic design, Genetic algorithm

Introduction

While projecting on the future of renewable energy, it is inevitable to include innovations in algorithmic thinking and artificial intelligence, and how it is contributing toward more applicable and efficient designs. Solar singularity has become a scientific obsession to reach a time when solar energy is the cheapest and most reliable source of power, and research have been on the right path toward this world-changing achievement (Hunt 2018).

One of the key topics of interest in solar technology is non-imaging optics (O'Gallagher 2008), where refractive and reflective systems are employed to concentrate and collect solar heat, which is then utilized in a vast variety of applications. Superiority of refractive Fresnel lenses over parabolic reflectors lies not only in the lower weight and cost, but also in the efficient performance that can produce ultra-high temperatures, with a compact design that requires less shape maintenance (Kumar et al. 2015).

The use of Fresnel lenses as solar concentrators dates back to the 1950s, with the main focus being solar power generation (Xie et al. 2011) and concentrated photovoltaics (Kumar et al. 2015). Other applications were also considered, from hydrogen generation and photo-bioreactors, to metallic surfaces' modification and solar lighting (Xie et al. 2011).

Solar welding research have been, for the most part, analyzing the use of reflective optical systems in metal fabrication. Karalis et al. (2005) and Pantelis et al. (2017a, b) welded 3-mm-thick aluminum plates and 1.3-mm-thick titanium-alloy sheets utilizing a solar furnace comprising a heliostat, an attenuator, and a parabolic concentrator that produces a 7000 kW/m^2 flux on a 12-cm-diameter focus. A similar furnace with a 2-kW 1.5-m-diameter parabolic concentrator was used by Romero et al. (2015) to weld 5-mm-thick titanium-alloy specimens. Welding of 25-mm-thick aluminum-foam plates was achieved by Cambronero et al. (2014) utilizing a 58-kW solar furnace, with a 300-W/cm^2 peak flux at a 26-cm-diameter focus under a 1000-W/m^2 irradiation.

Small-scale solar welding has also been researched for low-temperature applications. Alami and Aokal (2017)

*Correspondence: weihuan.zhao@unt.edu
[1] Mechanical and Energy Engineering Department, College of Engineering, University of North Texas, Denton, TX 76207, USA
Full list of author information is available at the end of the article

used a 20-cm-diameter crystal sphere with a 0.8-mm-diameter focus to weld 1-mm-thick Poly-methyl-meth-acrylate PMMA specimens.

Similarly, parabolic dishes have been utilized in the majority of solar Stirling engine systems. Barreto and Canhoto (2017) achieved about 20% overall engine efficiency when simulated with a 95% optically efficient parabolic dish. Beltrán-Chacon et al. (2015) analyzed the influence of a variable dead-volume on the solar Stirling engine performance and simulated a net energy conversion efficiency of 23.4%. Hafez et al. (2016) created a MATLAB®-based simulation and modeling tool for the parabolic dish–Solar Stirling engine system. Li et al. (2011) studied the temperature and solar flux of a parabolic dish–Stirling engine system, simulating it with both CFD (Computational Fluid Dynamics) and MCRT (Monte-Carlo Ray Tracing) methods, and validating the simulation experimentally with a 7 kW Xenon-lamp solar simulator. Ahmadi et al. (2013) algorithmically optimized the output power and overall thermal efficiency of a solar dish–Stirling engine system while minimizing the entropy generation rate.

Few works have implemented the use of Fresnel lenses to supply Stirling engines with solar heat. Acharya and Bhattacharjee (2014) enclosed the Stirling engine heater with a capsule that has its upper hemisphere made up of Fresnel lenses. Cheng et al. (2016) achieved 718 °C on the heater of a Stirling engine with a biaxially tracked 1.3 m × 0.9 m Fresnel lens. Zhong et al. (2017) modeled a solar Stirling engine system for space applications where concentrated sunlight from a Fresnel lens will change its direction through an optical fiber bundle.

Besides the fact that most designs have focused on the use of reflective means, rather than refractive, to collect and concentrate solar energy for thermal applications, another missing factor is the lack of application-based designs of the solar concentrator to match a desired thermal output.

A reverse-engineering point of view will be adopted in this work, matching an optimum deign of the Fresnel lens solar concentrator to the thermal and geometrical requirements of various applications through an algorithm, and verifying this algorithmically optimized system through ray-optics and heat transfer simulations. This fine-tuning process aims to efficiently utilize energy, space, materials and resources, while reducing the initial costs and maximizing the optical efficiency.

Analytical methods

Required solar heat estimation

The first step into the concentrator design is estimating the total required solar heat to be supplied focally to the receiver $\dot{Q}_{req}$. Here, two sources of heat dissipation are considered:

1. Focal heat loss $\dot{Q}_{loss}$: Heat lost from the lens' focal area due to convection and radiation. It is calculated by the algorithmically implemented relations and tables from Bergman et al. (2011), based on the desired focal properties like material, diameter, temperature and ambient conditions.
2. Application heat $\dot{Q}_{app}$: Heat utilized by the application. Non-focal heat losses are also considered part of the application heat. $\dot{Q}_{app}$ is estimated manually by the user according to the specific geometry and energy requirements of the application.

Then, the total required solar heat $\dot{Q}_{req}$ at the receiver is found as

$$\dot{Q}_{req} = \dot{Q}_{loss} + \dot{Q}_{app} \quad [W]. \tag{1}$$

Genetic-themed hierarchical algorithm (GTHA)

Once $\dot{Q}_{req}$ is obtained, a genetic-themed hierarchical algorithm (GTHA) evaluates the optimum lens geometry, represented by the lens diameter D_l, focal length f and number of prismatic grooves g. The following terms used to express the algorithm's structuring and flow are similar to those used by the Evolutionary Genetic Algorithms (Mitchell 1998), hence termed as "Genetic-themed". It is worth mentioning that all analyses and calculations are based on a solar flux that is normally incident on the lens, which requires dual-axis tracking of the sun.

The GTHA is constructed of five hierarchical layers, as illustrated in Fig. 1, the highest $L1$ representing the lens optical efficiency η_l, followed by $L2$ for the sampling margin $S, L3$ for the lens diameter D_l, $L4$ for the focal length f, and $L5$ for the number of equal-width prism grooves
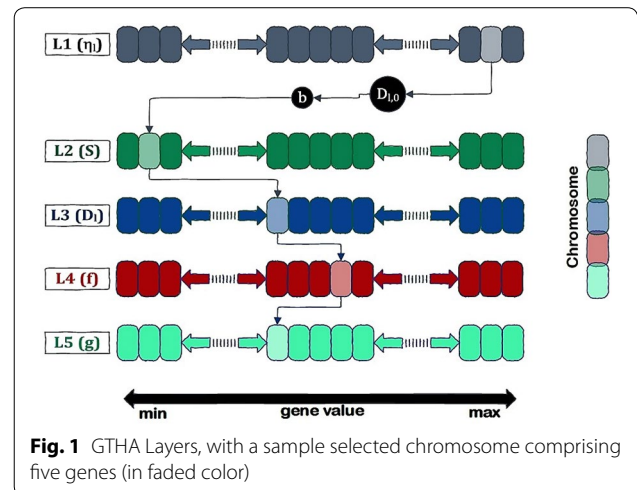

Fig. 1 GTHA Layers, with a sample selected chromosome comprising five genes (in faded color)

g. Each single value in a layer is called a gene, and each iterational data set is called a chromosome and comprises five genes, one from each layer. Both *L1* and *L2* have genes in the form of fractions, with a 0.95 maximum and a 0.10 minimum, decrementing (for *L1*) or incrementing (for *L2*) in the steps of 0.05.

The algorithmic search for the optimum lens geometry begins with an initial guess of the lens diameter $D_{l,0}$, rounded to the nearest integer and taken at a local solar irradiance $I_{b,N}$ in W/m^2 and an iterated value of η_l from the lens efficiency layer *L1*;

$$D_{l,0} = \text{Round}\left[\left(\frac{4\dot{Q}_{req}}{\eta_l \pi I_{b.N}}\right)^{1/2} \times 10^3, 0\right] \text{ [mm].}$$

(2)

This $D_{l,0}$ value is then used to size *L3*, *L4* and *L5* populations depending on an iterated fraction from layer *L2* called the sampling margin *S*, which evaluates each level's bounding limits. Noting that an optimum focal length *f* is predicted equal to the lens diameter D_l (Victoria et al. 2016). While an optimum number of grooves *g* is anticipated equal to $0.25D_l$ in this work, balancing manufacturing limitations and transmission losses (Leutz and Suzuki 2001). Thus, level sizing can be obtained in an iterational formatting that shows the upper and lower bounds and step size as

2. Selection:

- An initial "zeroth" chromosome is constructed by selecting the lowest gene in each of *L3*, *L4* and *L5* hierarchy layers.
- All subsequent gene selections are done on an incremental basis for *L3*, *L4* and *L5*. Each with the corresponding step size indicated earlier by Eqs. 3–5.

3. Fitness function check and convergence:

- The chromosome genes are used to find the lens' prismatic geometry and evaluate the actual focused heat $\dot{Q}_f$, then compare it to the required focal heat $\dot{Q}_{req}$. An earlier work of the authors is employed for this purpose (Qandil and Zhao 2018), which is briefly summarized after this terminology explanation.
- If $\dot{Q}_f \geq \dot{Q}_{req}$, the algorithm converges and outputs:

  a. The current values of *L3*, *L4* and *L5* as optimum.
  b. The lens' prism angles θ and prism heights *h*.
  c. The focal heat flux $\dot{Q}_f$ distribution, with 2D and 3D graphics.

$$L3(D_l) = \left\{\text{Round}\left[(1-S)D_{l,0}, 0\right] : \text{Round}\left[\frac{2SD_{l,0}}{10}, 0\right] : \text{Round}\left[(1+S)D_{l,0}, 0\right]\right\} \text{ [mm],}$$

(3)

$$L4(f) = \left\{\text{Round}[(1-S)(L3), 0] : \text{Round}\left[\frac{2S(L3)}{10}, 0\right] : \text{Round}[(1+S)(L3), 0]\right\} \text{ [mm],}$$

(4)

$$L5(g) = \left\{\text{Round}[0.25(1-S)(L3), 0] : \text{Round}\left[\frac{S(L3)}{20}, 0\right] : \text{Round}[0.25(1+S)(L3), 0]\right\}.$$

(5)

Initializing the GTHA does not happen randomly, since minimizing the lens geometry is a desired aspect; hence, the operation of the algorithm illustrated in Fig. 2 can be summarized in a genetic-algorithm terminology as

1. Initial population:

- The required focal heat $\dot{Q}_{req}$ is calculated, then used with the maximum *L1* value of optical efficiency η_l to evaluate $D_{l,0}$.
- The minimum *L2* value of the sampling margin *S* is used to size *L3*, *L4* and *L5* populations.

d. The actual optical efficiency $\eta_{l,a}$ and lens transmittance *T*. Noting that the calculated actual efficiency $\eta_{l,a}$ can differ from the iterated efficiency in layer *L1*, since the iterated efficiency is only used to find the initial guess $D_{l,0}$, while the calculated efficiency is found at the optimum geometrical parameters incorporated in Qandil and Zhao's (2018) statistical algorithm.

4. Mutation:

- Single mutation: If $\dot{Q}_{req}$ is not met by the zeroth chromosome, successive chromosomes are
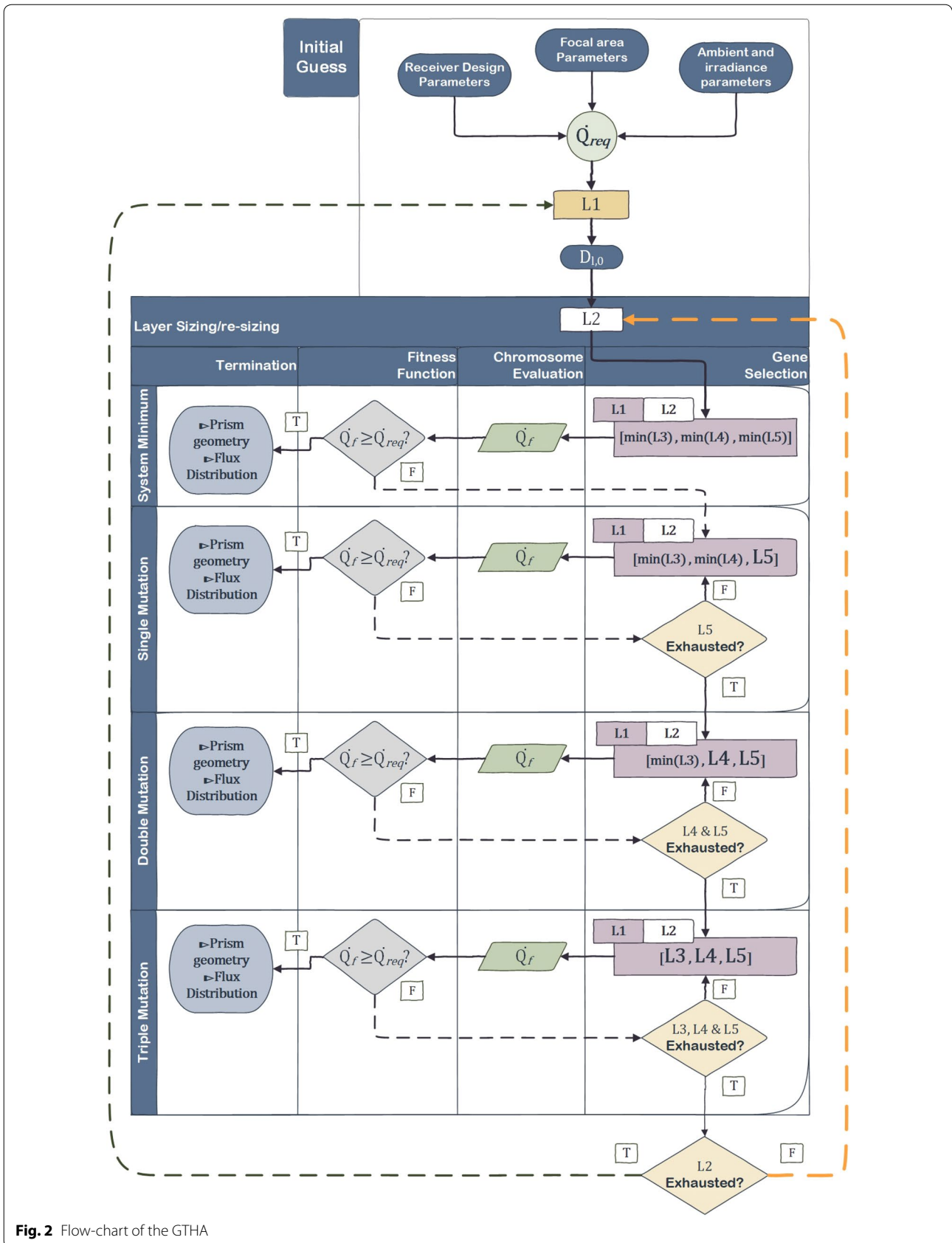
Fig. 2 Flow-chart of the GTHA

mutated by incrementing the lowest layer gene $L5$ without replacement until convergence.

- Double mutation: If $L5$ genes are exhausted without convergence, successive chromosomes are mutated by incrementing $L4$, then $L5$ genes until convergence.
- Triple-mutation: Similarly, if both $L4$ and $L5$ genes are exhausted before convergence, the $L3$ gene will start incrementing as well until convergence.

5. Re-sizing:

- If all $L3$, $L4$ and $L5$ layer genes were exhausted without convergence, the layers are re-sized by incrementing the sampling margin gene $L2$, which results in the new layer boundaries that restart the mutation process in *step 4* until convergence.

6. Re-initiation:

- If re-sizing UnOrderedList-Bullet-Start_Sub1 all $L2$ genes without convergence, the initial guess $D_{l,0}$ is re-evaluated with a decremented value of the optical efficiency gene $L1$, and the process is repeated from *step 1* until convergence.

If spatial constraints exist, system parameters can be limited to certain ranges, especially while incrementing the lens diameter and focal length genes.

As stated earlier in the terminology point 3, for each nth chromosome $[\eta_l, S, D_l, f, g]_n$, an algorithm employing the statistical concept of light refraction by Qandil and Zhao (2018) evaluates the corresponding received heat at the predetermined focal spot area. It assumes a statistically in equilibrium light comprising 10^{12} rays per unit area, each incident in a large number of states due to different combinations of incidence conditions. The algorithm divides the receiver into symmetrical segments, and traces all rays onto the receiver while counting and successful ray arrivals within each segment. The resulting density function of ray count is converted into a focal flux distribution $\dot{Q}_f$.

Results and discussion

To verify the validity of the GTHA-based lens design, two experimental applications were selected from the literature. A solar welding system that originally employs a solar furnace to concentrate solar energy (Romero et al. 2013), and a Stirling engine that was modified with a receiver cavity attached to the displacer cylinder on one side, and exposed to the concentrated solar energy from a Fresnel lens on the other (Aksoy and Karabulut 2013). The resulting optimum lens designs by the GTHA were

simulated, and its performance was compared to the literature experimental results.

Solar welding system

Romero et al. (2013) employed a solar furnace with a 1.5-m-diameter parabolic reflector to weld AISI H13 steel and 316-L stainless steel specimens. The reflector had a 15 mm focal diameter at 85 cm focal length. Specimens were welded in three joint designs, from which the single-V butt-welding of two $30 \times 60 \times 5$ mm^3 H13 steel specimens was selected for analysis in this work.

The GTHA was based on a 1530 °C (1803 K) focal surface temperature, taken as the melting point of H13 steel (Romero et al. 2013). A solar radiation of 700 W/m^2 is to be focused, as per the original work of Romero et al. (2013). The ambient temperature is assumed at 27 °C, and all thermal and physical properties of the H13 steel in this work are summarized in Table 1.

The cross-sectional macrograph of Romero et al. (2013) was used in modeling the required welding heat, where three zones, shown in Fig. 3, were considered for simplicity:

1. *Zone-1: The heat-affected zone (HAZ)* with a minimum surface temperature of 1010 °C, equal to the H13 steel austenization temperature (Romero et al. 2013). Heat loss from this zone is the focal heat loss $\dot{Q}_{loss}$.
2. *Zone-2: The transition zone* between the *HAZ* and the melting zone, assumed at an average temperature of 1355 °C, extending 11.25 mm radially from the edge of the melting zone. Heat loss from this zone is also accounted for by the application heat $\dot{Q}_{app}$.
3. *Zone-3: The melting zone* taken as the 15-mm-diameter focal spot, positioned at the center of the welding line. A minimum surface temperature of 1700 °C was used here, higher than the melting temperature to act as a safety margin compensating for unaccounted losses. Heat loss from this zone is accounted for by the application heat $\dot{Q}_{app}$.

Table 1 Used thermal and mechanical properties of H13 steel

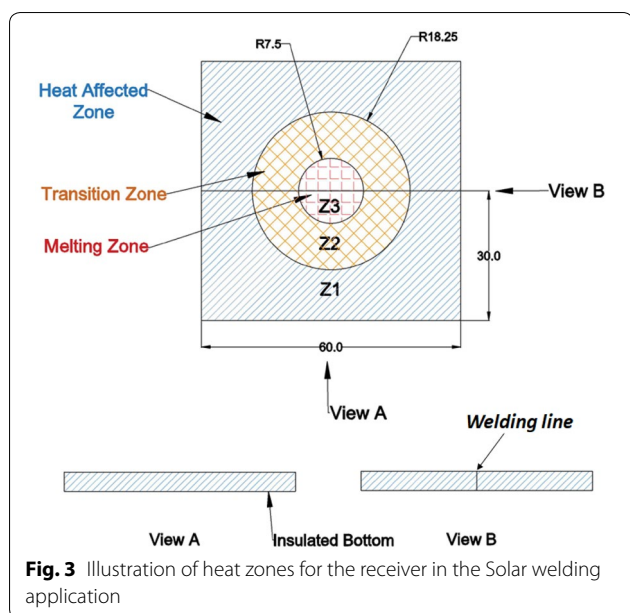|	
Melting temperature (Romero et al. 2013)	1530 °C (1803 K)
Austenization temperature (Romero et al. 2013)	1010 °C
Emissivity (Marashi et al. 2017)	0.8
Density (Iron Boar Labs Ltd 2009)	7800 kg/m^3
Latent heat of fusion (Iron Boar Labs Ltd 2009)	270 kJ/kg
Specific heat capacity (Iron Boar Labs Ltd 2009)	470 J/kg·K
Thermal conductivity (Iron Boar Labs Ltd 2009)	29 W/m·K

Fig. 3 Illustration of heat zones for the receiver in the Solar welding application

Table 2 Values of converging chromosome genes from the GTHA), and the optimum lens performance parameters from the statistical algorithm (Qandil and Zhao 2018) for the Solar welding application

Variable		Value	Source
$L1(\eta_l)$	Lens efficiency (initial guess)	0.95	GTHA
$L2(S)$	Sampling margin	0.10	GTHA
$D_{l,0}$	Initial guess of lens diameter	1109 mm	GTHA
$L3(D_l)$	Lens diameter	1198 mm	GTHA
$L4(f)$	Focal length	1150 mm	GTHA
$L5(g)$	Number of grooves	285	GTHA
$\dot{Q}_f$	Total focal energy received	646.9 W	Qandil and Zhao (2018)
T	Lens transmittance	93.54%	Qandil and Zhao (2018)
$\eta_{l,a}$	Actual optical efficiency	82.03%	Qandil and Zhao (2018)
η_o	Overall lens efficiency	76.73%	Qandil and Zhao (2018)

Radiation-only heat loss was considered for all zones, with the bottom surface assumed insulated. The system variables inputted into the GTHA returned a total required focal heat $\dot{Q}_{req}$ of 644 W.

The GTHA incorporated in MATLAB® converged at the algorithmic chromosome genes listed in Table 2. When it was synched to the statistical algorithm of Qandil and Zhao (2018), the optimum chromosome returned the Poly-methyl-methacrylate (PMMA) Fresnel concentrator dimensions and performance parameters displayed in Table 2.

The aperture area of the optimum lens from Table 2 is 36.2% less than that of the parabolic trough used by Romero et al. (2013), which reflects a significant decrease in the concentrator size, with only 35.3% increase in the focal distance. The statistical algorithm also outputted the symmetrical focal–flux distribution in Fig. 4a, represented by a 3D third-order Gaussian function plotted against the focal area in Fig. 4b. The corresponding optimum dimensions of the 2.1-mm equal-width prismatic grooves are displayed in Fig. 5, with groove numbers ascending away from the center.
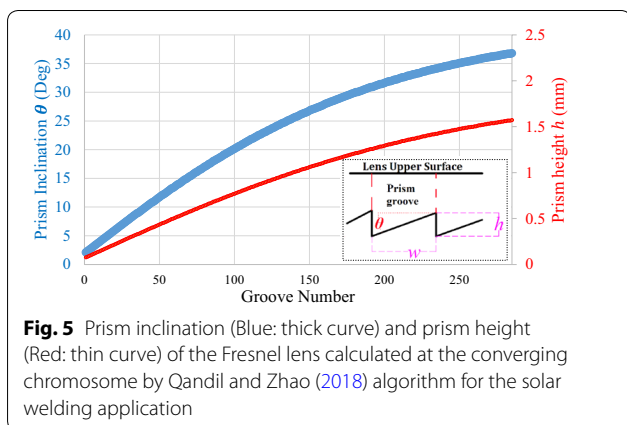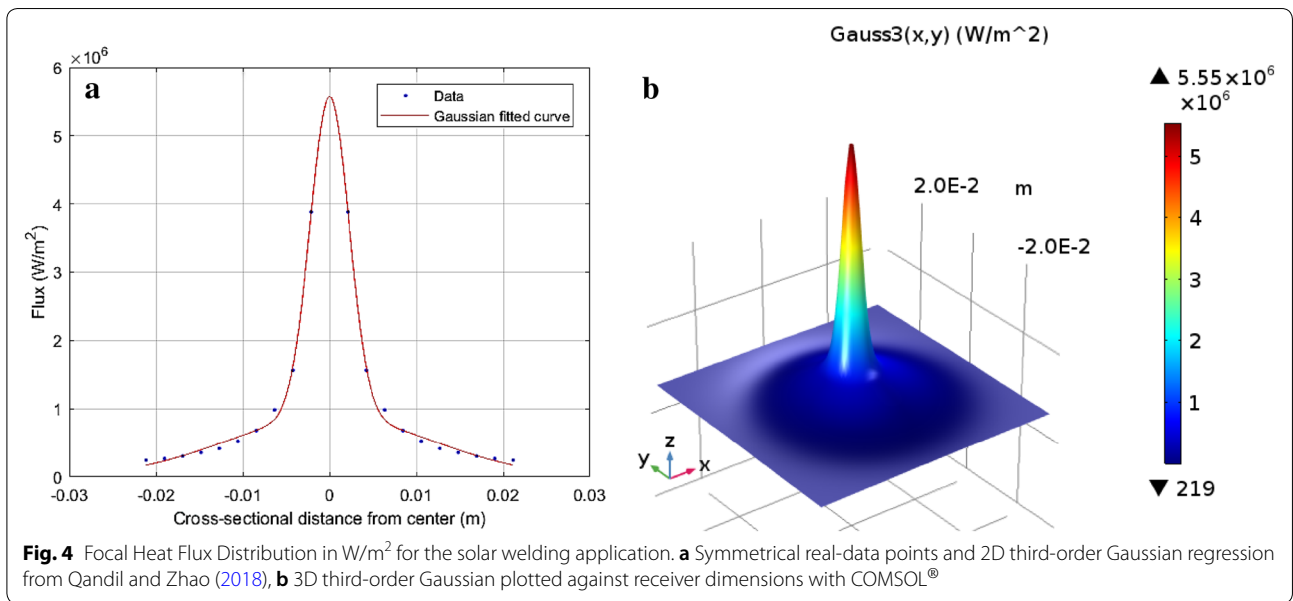
Once the optimum lens was modeled with 3D AutoCAD®, a Monte-Carlo Ray-Tracing (MCRT) simulation was conducted via COMSOL Multiphasics®, with the setup shown in Fig. 6a. An intensity of 10,000 solar rays can be seen converging onto the focal plane in Fig. 6b.

Ray-heating simulation was conducted in a vacuum ambient with radiation losses only. The bottom surface of the welded specimens was assumed insulated, which can be achieved in practice by a high-temperature graphite-insulation board (CeraMaterials 2018) placed on top of the welding table. The focal spot was positioned at the assembly's midpoint, and the flat weld-line was considered with no filler rod for simplicity. Figure 7a shows the assembly's converging temperature distribution at 120 s, while Fig. 7b plots both the average focal area temperature and the temperature of the assembly's bottom central point over the simulation time, up until convergence.

It can be noted from Fig. 7b that the 15-mm-diameter focal area will reach the melting temperature (1803 K) within about 90 s, which means, in order for each surface point on the weld-line to melt, it will need to be exposed to the focal heat for at least 90 s. This corresponds to maximum tracking speed of 0.167 mm/s for the welding process (15 mm ÷ 90 s), about 44.4% slower than the 0.3 mm/s speed used by Romero et al. (2013). Figure 7b also shows that the molten metal temperature reaches steady state after 120 s of exposure to solar heat.

Heat propagation with time through the assembly's thickness is displayed in Fig. 8a–d with heat maps at increments of 30 s for a longitudinal cross-section of the welded specimen. Figure 8b shows the beginning of surface melting at 60 s, and Fig. 8c depicts a half-way penetration of the molten state at 90 s, which becomes fully penetrated within 120 s in Fig. 8d.
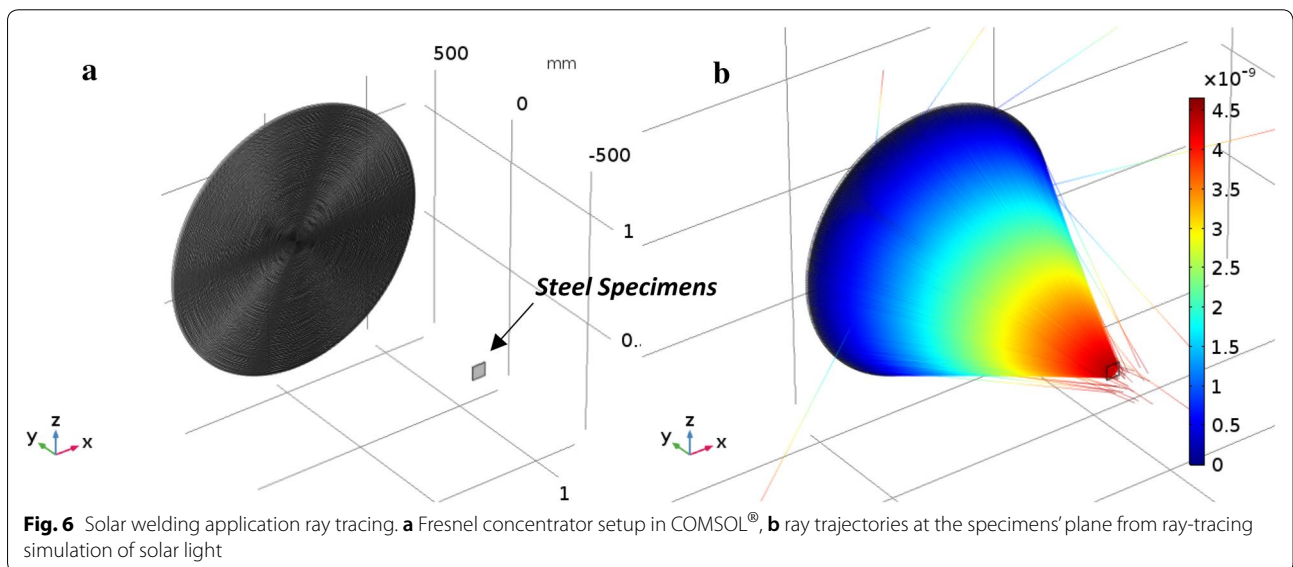
While the Fresnel lens showed comparable welding speed to the literature work, a considerable decrease is noted in the aperture diameter of the Fresnel lens compared to the parabolic reflector of Romero et al. (2013). Adding the design simplicity of the lens concentrator in comparison to the multi-reflection system of the solar furnace (Shanks et al. 2016), and the low-cost

Fig. 4 Focal Heat Flux Distribution in W/m² for the solar welding application. **a** Symmetrical real-data points and 2D third-order Gaussian regression from Qandil and Zhao (2018), **b** 3D third-order Gaussian plotted against receiver dimensions with COMSOL®

Fig. 5 Prism inclination (Blue: thick curve) and prism height (Red: thin curve) of the Fresnel lens calculated at the converging chromosome by Qandil and Zhao (2018) algorithm for the solar welding application
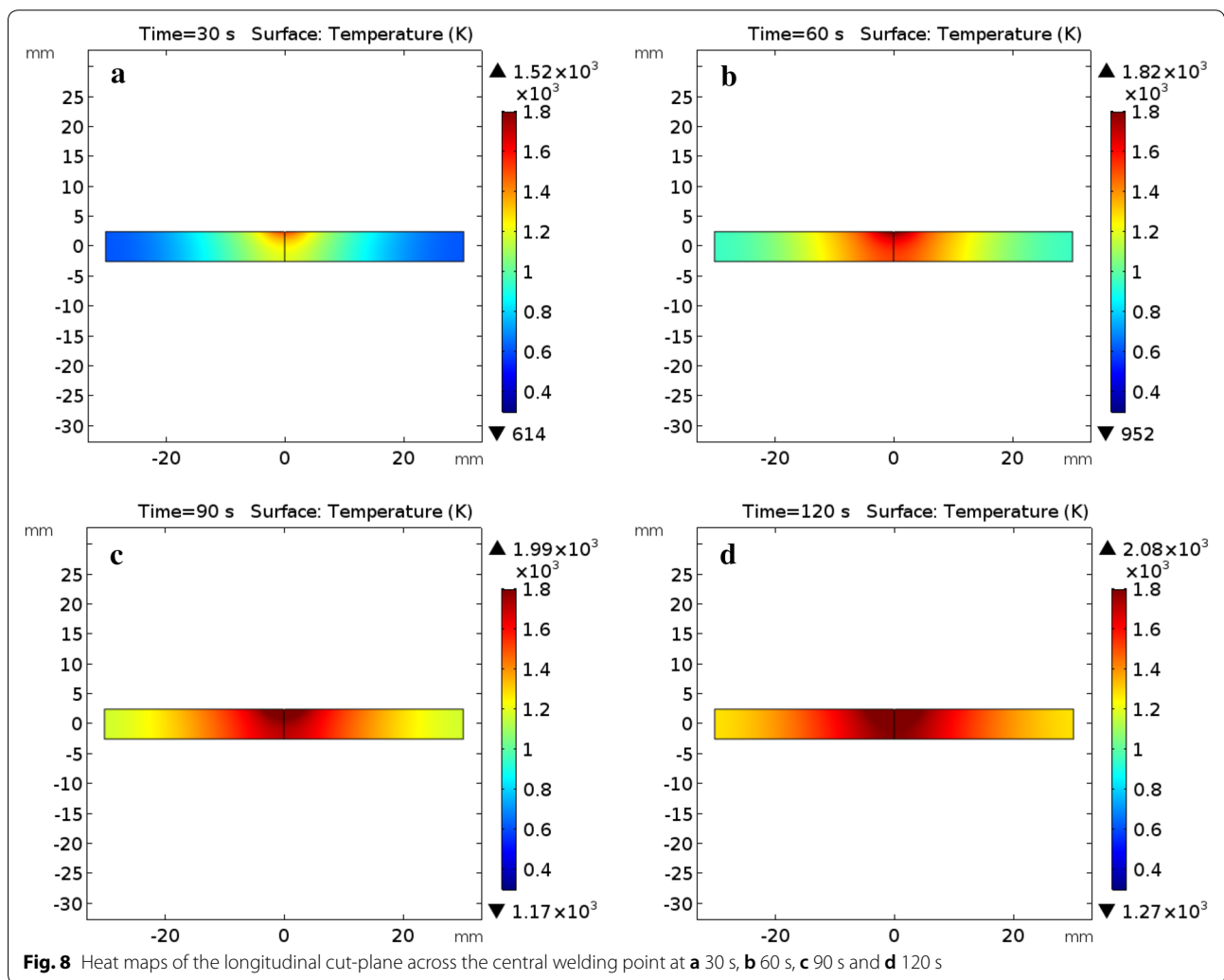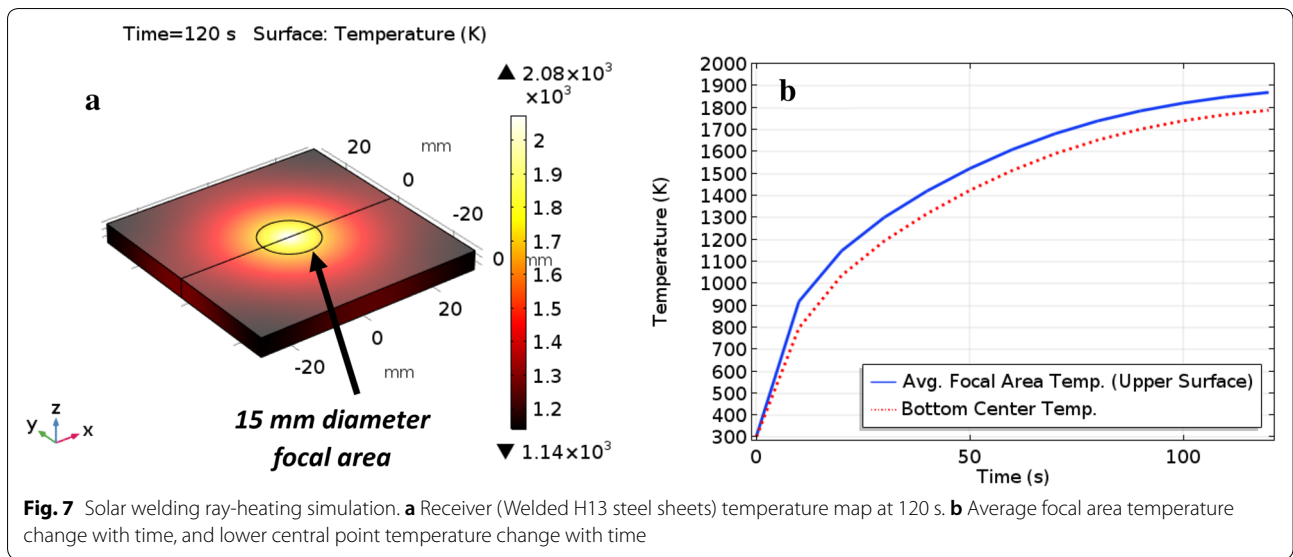
manufacturing of the PMMA acrylic resin lens via injection-molding or casting processes, all can undoubtedly reduce the capital cost of the solar welding system.

Solar-powered Stirling engine

Another promising application of a Fresnel concentrator is providing high heat flux to Stirling engines. The work of Aksoy and Karabulut (2013), considered for this comparative analysis, used a 1.4-m² Fresnel lens to concentrate solar heat on a cavity attached at the top of the displacer cylinder. Three cavities made of different metals were used, among which aluminum was found to provide

Fig. 6 Solar welding application ray tracing. **a** Fresnel concentrator setup in COMSOL®, **b** ray trajectories at the specimens' plane from ray-tracing simulation of solar light

Fig. 7 Solar welding ray-heating simulation. **a** Receiver (Welded H13 steel sheets) temperature map at 120 s. **b** Average focal area temperature change with time, and lower central point temperature change with time

Fig. 8 Heat maps of the longitudinal cut-plane across the central welding point at **a** 30 s, **b** 60 s, **c** 90 s and **d** 120 s

the highest performance (Aksoy and Karabulut 2013), hence analyzed in this work.

Since the purpose of using a cavity is to maximize and trap the collected focal heat, it can be equivalently replaced by a blackbody surface. Thus, as shown in Fig. 12a, this work will only use the 100-mm-diameter cavity base (bottom wall) of the reference design of Aksoy and Karabulut (2013) as a focal blackbody receiver, while discarding the side walls.

The design temperature of the focal surface is taken at 425 °C, equal to the bottom wall temperature of the aluminum cavity in the referenced work at a solar radiation of 816 W/m^2 (Aksoy and Karabulut 2013). The ambient temperature was assumed at 27 °C, and the heater section of the displacer cylinder was wrapped with a 40-mm-thick ceramic-fiber blanket to reduce thermal losses as per the referenced work (Aksoy and Karabulut 2013). Table 3 lists all used design properties of the aluminum and the fiber blanket in both the GTHA and COMSOL® simulations.

The solar energy input of Aksoy and Karabulut's (2013) experiment was 1142 W, which is all used in this work as application heat $\dot{Q}_{app}$ delivered from the inner walls of the receiver to the working fluid. An additional 136.6 W of focal radiative and convective losses $\dot{Q}_{loss}$ were algorithmically calculated, resulting in a 1278.6 W of total solar heat required focally $\dot{Q}_{req}$. The GTHA returned the optimum Fresnel concentrator characteristics listed in Table 4, with the focal heat flux distribution plotted as a second-order Gaussian function in 2D and 3D in Fig. 9a, b.

A 22.7% increase in the lens area is noticeable compared to that used by Aksoy and Karabulut (2013). This is expected since all their 1142 W of focally received solar heat was considered in this work as fully utilized application heat delivered at the inner walls of the heater. Therefore, more lens area was required to compensate for the extra 136.6 W of focal heat losses calculated by the GTHA.

Prismatic dimensions for each of the 333 grooves are plotted in Fig. 10, with groove numbers ascending away from the center. Figure 11a exhibits the setup for the lens

Table 4 Values of converging chromosome genes from the GTHA), and the optimum lens performance parameters from the statistical algorithm (Qandil and Zhao 2018) for the Stirling engine application

Variable		Value	Source
$L1 (\eta_l)$	Lens efficiency (initial guess)	0.95	GTHA
$L2 (S)$	Sampling margin	0.10	GTHA
$D_{l,0}$	Initial guess of lens diameter	1450 mm	GTHA
$L3 (D_l)$	Lens diameter	1479 mm	GTHA
$L4 (f)$	Focal length	1331 mm	GTHA
$L5 (g)$	Number of grooves	333	GTHA
$\dot{Q}_f$	Total focal energy received	1317.12 W	Qandil and Zhao (2018)
T	Lens transmittance	92.49%	Qandil and Zhao (2018)
$\eta_{l,a}$	Actual optical efficiency	93.95%	Qandil and Zhao (2018)
η_o	Overall lens efficiency	86.90%	Qandil and Zhao (2018)

and the insulated heater positioned at 1.33 m focal distance. Figure 11b shows the ray convergence onto the focal area.

Heat transfer simulation for the receiver, i.e., the aluminum heater wrapped with the ceramic-fiber blanket, was conducted by COMSOL® considering both convective and radiative heat losses, with the application heat continuously depleted from the inner heater walls.
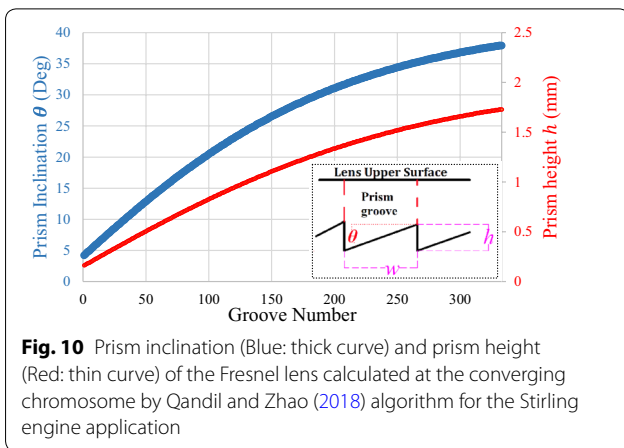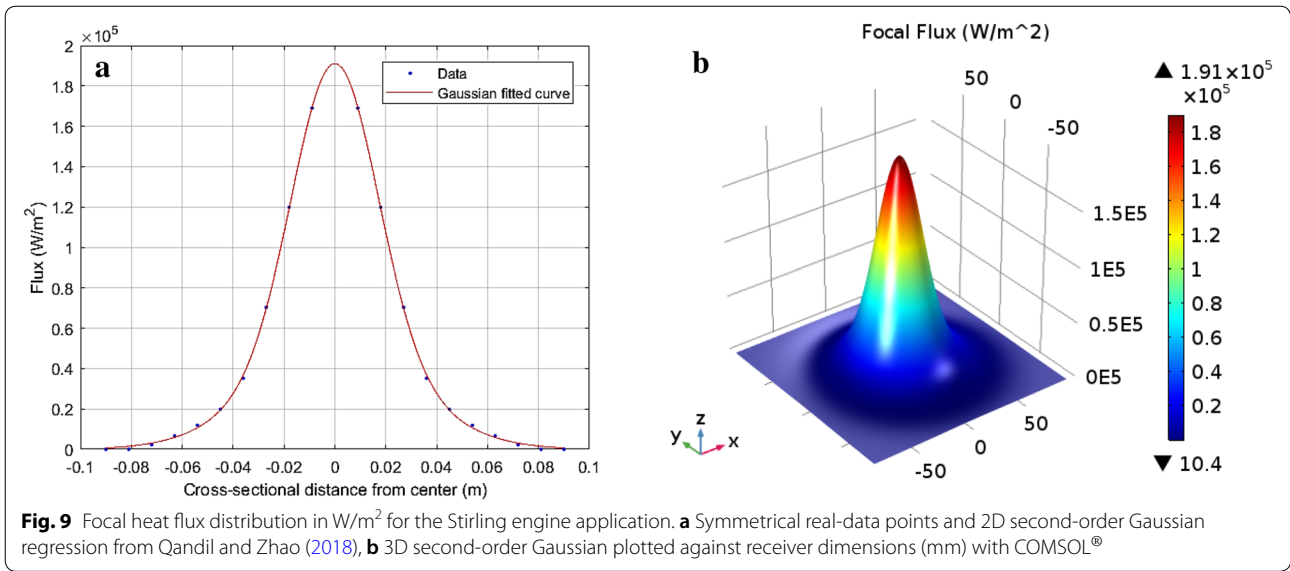
The receiver heat map at steady state is shown in Fig. 12a, where a maximum temperature at the center of the upper surface (facing the lens) converged to about 885 K after 2400 s, depicted in Fig. 12b. The 698 K (425 °C) desired cavity-base temperature of the (Aksoy and Karabulut 2013) design was reached in about 820 s, and the steady-state receiver temperature was still below the melting point of Aluminum, i.e., 923 K (650 °C) (Iron Boar Labs Ltd 2009).

Symmetrical heat maps of a central longitudinal cut-plane of the receiver, up to steady state, are visualized in Fig. 13a–c. The outer surface of the heat blanket remains

Table 3 Used thermal and mechanical properties of the aluminum heater and ceramic-fiber blanket

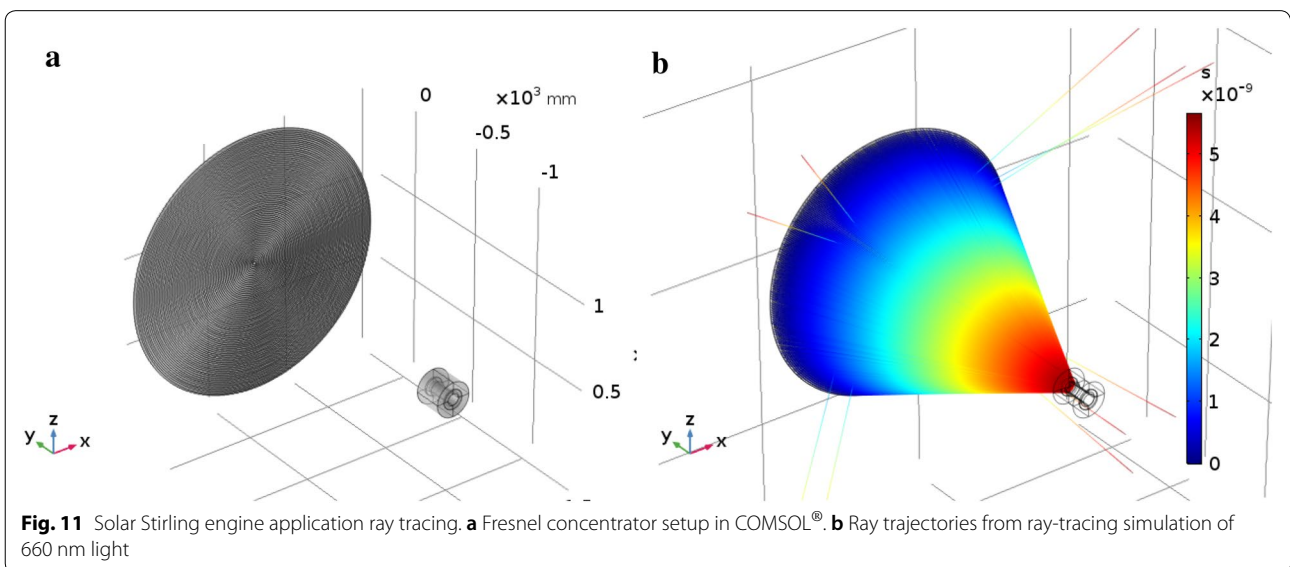| Aluminum	Emissivity (Blackbody)	1
	Density (Iron Boar Labs Ltd 2009)	2700 kg/m^3
	Specific heat capacity (Iron Boar Labs Ltd 2009)	904 J/kg·K
	Thermal conductivity (Iron Boar Labs Ltd 2009)	273 W/m·K
Ceramic-fiber blanket[a]	Emissivity	0.9
	Density	128 kg/m^3
	Specific heat capacity	1130 J/kg·K
	Thermal conductivity	0.08 W/m·K

[a] Properties based on product information sheet of Kaowool™ Blanket SZr in density of 8 PCF by Morgan Advanced Materials Corp.

Fig. 9 Focal heat flux distribution in W/m^2 for the Stirling engine application. **a** Symmetrical real-data points and 2D second-order Gaussian regression from Qandil and Zhao (2018), **b** 3D second-order Gaussian plotted against receiver dimensions (mm) with COMSOL®

Fig. 10 Prism inclination (Blue: thick curve) and prism height (Red: thin curve) of the Fresnel lens calculated at the converging chromosome by Qandil and Zhao (2018) algorithm for the Stirling engine application

at ambient temperature at all times, and the lower surface of the aluminum heater converges to about 700 K. Further simulations and testing of the whole Stirling engine system would be advisable to determine the overall thermal efficiency, which is beyond the scope of this work that only focuses on solar energy concentration and collection.

Conclusions and future work

The genetic-themed hierarchical algorithm GTHA was used to find the design properties of the Fresnel lens solar concentrator, meeting the thermal requirements of heating-based applications. Two experimental studies were used to verify the optimization method, a solar welding
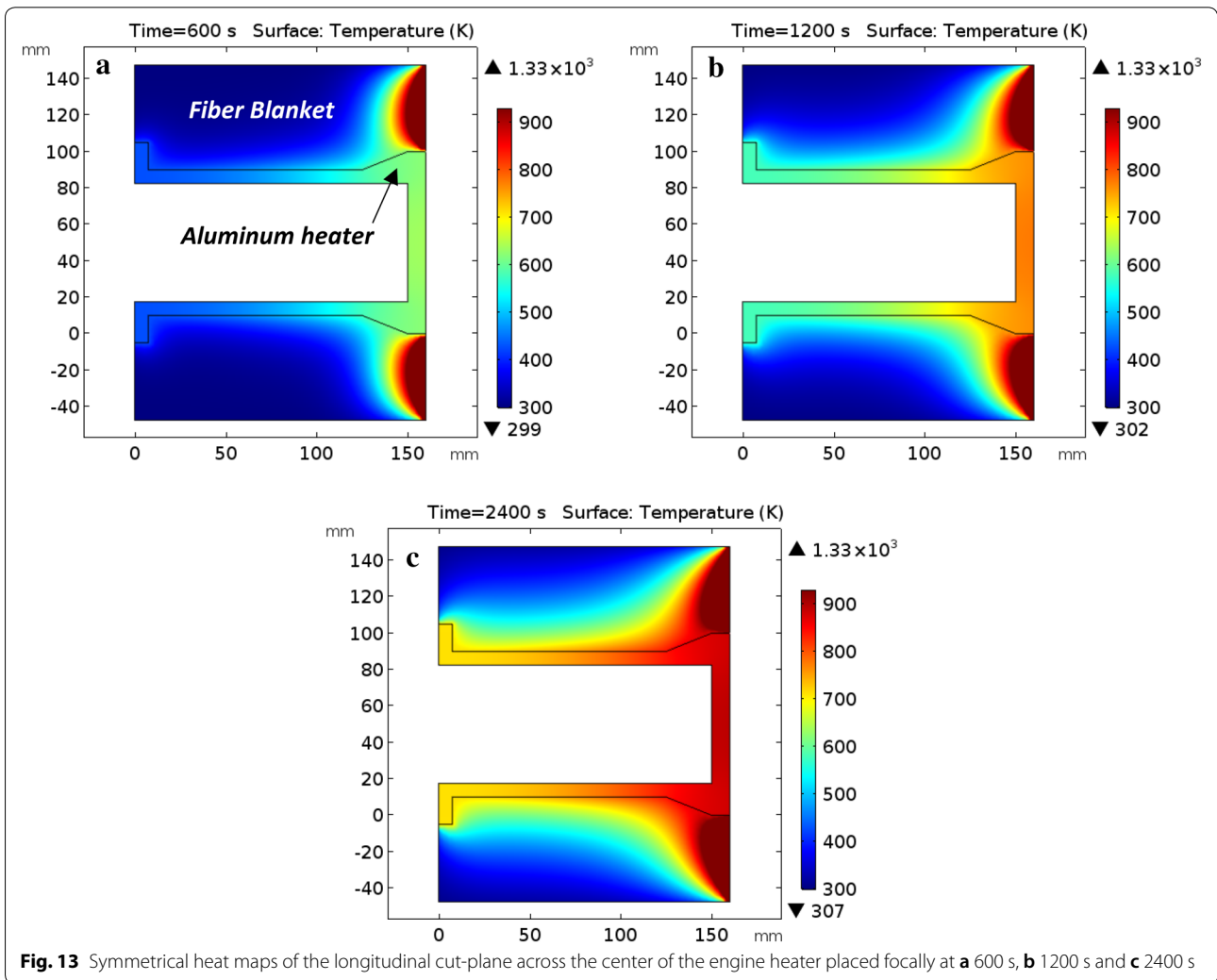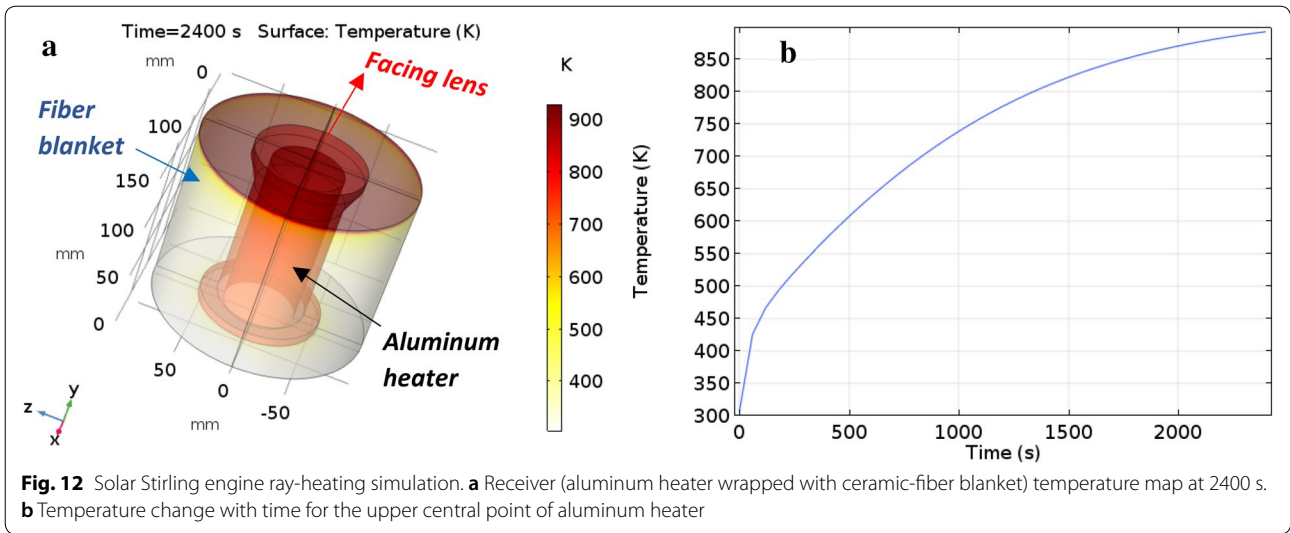

Fig. 11 Solar Stirling engine application ray tracing. **a** Fresnel concentrator setup in COMSOL®. **b** Ray trajectories from ray-tracing simulation of 660 nm light

Fig. 12 Solar Stirling engine ray-heating simulation. **a** Receiver (aluminum heater wrapped with ceramic-fiber blanket) temperature map at 2400 s. **b** Temperature change with time for the upper central point of aluminum heater

Fig. 13 Symmetrical heat maps of the longitudinal cut-plane across the center of the engine heater placed focally at **a** 600 s, **b** 1200 s and **c** 2400 s

Table 5 Comparative summary of this work for the two literature applications

Application	Solar welding		Solar stirling engine	
	Romero et al. (2013)	This work	Aksoy and Karabulut (2013)	This work
Concentrator type	Reflective Parabolic trough	Refractive Spot Fresnel lens	Refractive Spot Fresnel lens	Refractive Spot Fresnel lens
Receiver area	176.7 mm^2	176.7 mm^2	78.5 cm^2	78.5 cm^2
Irradiance	700 W/m^2	700 W/m^2	810 W/m^2	810 W/m^2
Concentrator Area	1.767 m^2	1.127 m^2	1.400 m^2	1.718 m^2
Specific application parameters	Welding speed		Solar heat input to the Stirling engine	
	0.3 mm/s	0.167 mm/s	1142 W	1317.12 W
	Total welding time		Receiver design	
	200 s	359 s	Cavity	Flat surface
Performance of this work for the referenced application	The lens has 36.2% smaller area with comparable welding quality (full penetration of molten state shown in Fig. 8) The acrylic lens is cheaper compared to the expensive parabolic trough furnace used in the literature The lens is lighter in weight and easier to install compared to the parabolic trough furnace used in the literature The slower welding speed of the lens system can be traded off by its cheaper and simpler design. System cost is a more pressing factor in many fabrication-level welding jobs than the welding time		Literature used a spot Fresnel lens, which is a good validation tool for this work's optimization This work simplified the receiver design from a cavity to a flat surface This work considered the 1142 W of energy received (reported by the literature) to be energy utilized in the simplified design. This increased the solar energy required, thus the bigger lens size This work's bigger lens supplied 15.34% more focal flux, and the engine reached steady operation without damaging the aluminum heater (Fig. 12b). Comparable to the operation achieved in the literature experiment The outer surface of the heat blanket remained at ambient temperature, same as in the literature experiment	

system and a solar Stirling engine system. Table 5 summarizes the findings of this work.

For future work, an ongoing research by the authors on lens fabrication aims to pick a real-life application and make the GTHA-optimized Fresnel lens that fits it. Then, experimentally verify the simulation results with real data.

List of symbols

A_l: lens area [m^2]; A_s: focal spot area [m^2]; C_{geo}: geometrical concentration ratio; D_l: lens aperture diameter [m]; $D_{l,0}$: initial guess of Lens aperture diameter [m]; f: focal length [m]; g: number of equal-width prism grooves; h: prism height [mm]; $I_{b,N}$: Beam solar irradiance [W/m^2]; L(): hierarchical layer order; $\dot{Q}_{app}$: heat to be used by the application [W]; $\dot{Q}_F$: focal heat supplied by the optimum lens [W]; $\dot{Q}_{loss}$: heat loss from the focal spot area [W]; $\dot{Q}_{req}$: total solar heat needed at the focal spot [W]; S: sampling margin [%]; T: lens transmittance [%].

Greek symbols

η_l: lens optical efficiency (used in GTHA) [%]; $\eta_{l,a}$: lens actual optical efficiency [%]; η_o: lens overall efficiency [%].

Authors' contributions
HQ developed the theory and performed the computations. SW and WZ supervised the findings of this work. All authors discussed the results and contributed to the final manuscript. All authors read and approved the final manuscript.

Availability of data and materials
Data sharing is not applicable to this article as no datasets were generated or analyzed during the current study.

Competing interests
The authors declare that they have no competing interests.

Author details
[1] Mechanical and Energy Engineering Department, College of Engineering, University of North Texas, Denton, TX 76207, USA. [2] Engineering Technology Department, College of Engineering, University of North Texas, Denton, TX 76207, USA.

References
Acharya, S., & Bhattacharjee, S. (2014). Stirling engine based solar–thermal power plant with a thermo-chemical storage system. *Energy Conversion and Management, 86,* 901–915. https://doi.org/10.1016/j.enconman.2014.06.030.
Ahmadi, M. H., Mohammadi, A. H., Dehghani, S., & Barranco-Jiménez, M. A. (2013). Multi-objective thermodynamic-based optimization of output power of solar dish–Stirling engine by implementing an evolutionary algorithm. *Energy Conversion and Management, 75,* 438–445. https://doi.org/10.1016/j.enconman.2013.06.030.

Aksoy, F., & Karabulut, H. (2013). Performance testing of a Fresnel/Stirling micro solar energy conversion system. *Energy Conversion and Management, 75,* 629–634. https://doi.org/10.1016/j.enconman.2013.08.001.

Alami, A., & Aokal, K. (2017). Experiments on polymer welding via concentrated solar energy. *International Journal of Advanced Manufacturing Technology, 92*(9–12), 3715. https://doi.org/10.1007/s00170-017-0431-x.

Barreto, G., & Canhoto, P. (2017). Modelling of a Stirling engine with parabolic dish for thermal to electric conversion of solar energy. *Energy Conversion and Management, 132,* 119–135. https://doi.org/10.1016/j.enconman.2016.11.011.

Beltrán-Chacon, R., Leal-Chavez, D., Sauceda, D., Pellegrini-Cervantes, M., & Borunda, M. (2015). Design and analysis of a dead volume control for a solar Stirling engine with induction generator. *Energy, 93,* 2593–2603. https://doi.org/10.1016/j.energy.2015.09.046.

Bergman, T. L., Lavine, A. S., Incropera, F. P., & DeWitt, D. P. (2011). *Introduction to heat transfer* (6th ed.). Hoboken, NJ: John Wiley & Sons Inc.

Cambronero, L. E. G., Cañadas, I., Ruiz-Román, J. M., Cisneros, M., & Corpas Iglesias, F. A. (2014). Weld structure of joined aluminium foams with concentrated solar energy. *Journal of Materials Processing Technology, 214*(11), 2637–2643. https://doi.org/10.1016/j.jmatprotec.2014.05.032.

CeraMaterials (2018). Carbon & Graphite Insulating Rigid Boards Database. http://www.ceramaterials.com. Accessed 16 November 2018.

Cheng, T., Yang, C., & Lin, I. (2016). Biaxial-type concentrated solar tracking system with a Fresnel lens for solar–thermal applications. *Applied Sciences, 6*(4), 115. https://doi.org/10.3390/app6040115.

Hafez, A. Z., Soliman, A., El-Metwally, K. A., & Ismail, I. M. (2016). Solar parabolic dish Stirling engine system design, simulation, and thermal analysis. *Energy Conversion and Management, 126,* 60–75. https://doi.org/10.1016/j.enconman.2016.07.067.

Hunt, T. (2018). The Solar Singularity: A status report on the global clean energy transition. *Greentech Media*. https://www.greentechmedia.com/articles/read/the-solar-singularity-trumped/.

Iron Boar Labs Ltd (2009). Material Properties Database. https://www.makeitfrom.com. Accessed 11 November 2018.

Karalis, D. G., Pantelis, D. I., & Papazoglou, V. J. (2005). On the investigation of 7075 aluminum alloy welding using concentrated solar energy. *Solar Energy Materials and Solar Cells, 86*(2), 145–163. https://doi.org/10.1016/j.solmat.2004.07.007.

Kumar, V., Shrivastava, R. L., & Untawale, S. P. (2015). Fresnel lens: a promising alternative of reflectors in concentrated solar power. *Renewable and Sustainable Energy Reviews, 44,* 376–390. https://doi.org/10.1016/j.rser.2014.12.006.

Leutz, R., & Suzuki, A. (2001). *Nonimaging fresnel lenses: Design and performance of solar concentrators.* New York City, New York: Springer. Retrieved from https://books.google.com/books?id=Z9-E5PhZCXMC.

Li, Z., Tang, D., Du, J., & Li, T. (2011). Study on the radiation flux and temperature distributions of the concentrator–receiver system in a solar dish/Stirling power facility. *Applied Thermal Engineering, 31*(10), 1780–1789. https://doi.org/10.1016/j.applthermaleng.2011.02.023.

Marashi, J., Yakushina, E., Xirouchakis, P., Zante, R., & Foster, J. (2017). An evaluation of H13 tool steel deformation in hot forging conditions. *Journal of Materials Processing Technology, 246,* 276–284. https://doi.org/10.1016/j.jmatprotec.2017.03.026.

Mitchell, M. (1998). *An introduction to genetic algorithms.* Cambridge, MA, USA: MIT Press.

O'Gallagher, J. (2008). *Nonimaging optics in solar energy*. San Rafael, Calif. 1537 Fourth Street, San Rafael, CA: Morgan & Claypool Publishers. Retrieved from https://doi.org/10.2200/S00120ED1V01Y200807EGY002.

Pantelis, D. I., Karakizis, P. N., Kazasidis, M. E., Karalis, D. G., & Rodrıguez, J. (2017a). Experimental and numerical investigation of AA6082-T6 thin plates welding using concentrated solar energy (CSE). *Solar Energy Materials and Solar Cells, 171,* 187–196. https://doi.org/10.1016/j.solmat.2017.06.063.

Pantelis, D. I., Kazasidis, M., & Karakizis, P. N. (2017b). Titanium alloys thin sheet welding with the use of concentrated solar energy. *Journal of Materials Engineering and Performance, 26*(12), 5760–5768. https://doi.org/10.1007/s11665-017-3049-0.

Qandil, H., & Zhao, W. (2018). Design and evaluation of the Fresnel-lens based solar concentrator system through a statistical–algorithmic approach. Paper presented at the *ASME 2018 International Mechanical Engineering Congress and Exposition.* Pittsburgh, Pennsylvania, USA. (52125) V08BT10A023. https://doi.org/10.1115/IMECE2018-87023.

Romero, A., García, I., Arenas, M. A., López, V., & Vázquez, A. (2013). High melting point metals welding by concentrated solar energy. *Solar Energy, 95,* 131–143. https://doi.org/10.1016/j.solener.2013.05.019.

Romero, A., García, I., Arenas, M. A., López, V., & Vázquez, A. (2015). Ti6Al4 V titanium alloy welded using concentrated solar energy. *Journal of Materials Processing Technology, 223,* 284–291. https://doi.org/10.1016/j.jmatprotec.2015.04.015.

Shanks, K., Senthilarasu, S., & Mallick, T. K. (2016). Optics for concentrating photovoltaics: trends, limits and opportunities for materials and design. *Renewable and Sustainable Energy Reviews, 60,* 394–407. https://doi.org/10.1016/j.rser.2016.01.089.

Victoria, M., Askins, S., Herrero, R., Antón, I., & Sala, G. (2016). Assessment of the optical efficiency of a primary lens to be used in a CPV system. *Solar Energy, 134,* 406–415. https://doi.org/10.1016/j.solener.2016.05.016.

Xie, W. T., Dai, Y. J., Wang, R. Z., & Sumathy, K. (2011). Concentrated solar energy applications using Fresnel lenses: a review. *Renewable and Sustainable Energy Reviews, 15*(6), 2588–2606. https://doi.org/10.1016/j.rser.2011.03.031.

Zhong, M., Li, Y., Mao, Y., Liang, Y., & Liu, J. (2017). Coupled optic–thermodynamic analysis of a novel wireless power transfer system using concentrated sunlight for space applications. *Applied Thermal Engineering, 115,* 1079–1088. https://doi.org/10.1016/j.applthermaleng.2017.01.052.

Publisher's Note